

A novel GPU-based sonar simulator for real-time applications

Abstract

Mainly when applied in the underwater environment, sonar simulation requires great computational effort due to the complexity of acoustic physics. Simulation of sonar operation allows evaluating algorithms and control systems without going to the real underwater environment; that reduces the costs and risks of in-field experiments. This paper tackles with the problem of real-time underwater imaging sonar simulation by using the OpenGL shading language chain on GPU. Our proposed system is able to simulate two main types of acoustic devices: mechanical scanning imaging sonars and forward-looking sonars. The underwater scenario simulation is performed based on three frameworks: (i) OpenSceneGraph reproduces the ocean visual effects, (ii) Gazebo deals with physical forces, and (iii) the Robot Construction Kit controls the sonar in underwater environments. Our system exploits the rasterization pipeline in order to simulate the sonar devices, which are simulated by means of three parameters: the pulse distance, the echo intensity and sonar field-of-view, being all calculated over objects shapes in the 3D rendered scene. Sonar-intrinsic operational parameters, speckle noise and object material properties are also considered as part of the acoustic image. **Our evaluation demonstrated that the proposed method is able to operate close to or faster than the real-world devices. Also, our method generates more visually realistic sonar images when compared with other approaches.**

Key words: Simulated sensor data, Sonar imaging, GPU-based processing, Robot Construction Kit (Rock), Underwater robotics.

1. Introduction

Simulation is an useful tool for designing and programming autonomous underwater vehicles (AUVs). That allows evaluating the vehicle behavior, without dealing with physical hardware or decision-making algorithms and control systems in real-time trials, as well as costly and time-consuming field experiments. AUVs usually demand expensive hardware and perform long-term data gathering operations, taking place in restrictive sites. When AUVs are not supported by an umbilical cable, and the underwater communication carries on by unreliable acoustic links, the vehicle should be able to make completely autonomous decisions, even with low-to-zero external assistance. While the analysis and interpretation of sensor data can be performed in a post-processing step, a real-time simulation is strongly necessary for testing and evaluation of vehicle's motion response, avoiding involved risks on real-world rides.

AUVs usually act below the photic zone, with high turbidity and huge light scattering. This makes the quality of image acquisition by optical devices limited by a short range, and artificially illuminated and clear visibility conditions. To tackle with that limitations, high-frequency sonars have been used primarily on AUVs' navigation and perception systems. Acoustic waves emitted by sonars are significantly less affected by water attenuation, aiding operation at greater ranges even as low-to-zero visibility conditions, with a fast refresh rate. Although sonar devices usually solve the main shortcomings of optical sensors in underwater conditions, they provide noisy data of lower resolution and more difficult interpretation.

By considering sonar benefits and singularities along with the need to evaluate AUVs, recent works proposed ray tracing- [1, 2, 3, 4, 5, 6] and tube tracing-based [7] techniques to simu-

late acoustic data with very accurate results, although presenting a high computational cost. Bell [1] proposed a simulator based on optical ray tracing for underwater side-scan sonar imagery; images are generated by acoustic signals represented by rays, which are repeatedly processed, forming a 2D-array. Coiras and Groen [2] used frequency-domain signal processing to produce synthetic aperture sonar frames; in that method, the acoustic image is created by computing the Fourier transform of the acoustic pulse used to insonify the scene. For forward-looking sonar simulations, Saç *et al.* [3] described a sonar model by computing the ray tracing in frequency domain; when a ray hits an object in 3D space, three parameters are calculated to process the acoustic data: the Euclidean distance from the sonar axis, the intensity of returned signal by Lambert illumination model and the surface normal; the reverberation and shadow phenomena are also considered in the scene rendering. DeMarco *et al.* [4] used Gazebo and Robot Operating System (ROS) [8] integration to simulate acoustic sound pulses by ray tracing technique, also producing a 3D point cloud of the coverage area; the reflected intensity takes into account the object reflectivity, and the amount of Gaussian and salt-and-pepper noises applied in the sonar image is empirically defined. Gu *et al.* [5] modeled a forward-looking sonar device, where the ultra-sound beams are formed by a set of rays; the acoustic image is significantly limited by a representation using only two colors: white, when the ray strikes an object, and black for shadow areas. Kwak *et al.* [6] improved the previous approach by adding a sound pressure attenuation to produce the gray-scale sonar frame, while the other physical characteristics related to sound transmission are disregarded. Guériot and Sintes [7] introduce a volume-based approach of energy interacting with the scene, and collected by the receiving sonar; the sound propagation is

64 defined by series of acoustic tubes, being always orthogonal to
 65 the current sonar view, where the reverberation and objects sur-
 66 face irregularities are also addressed.

67 1.1. Contributions

68 This paper introduces a novel imaging sonar simulator that
 69 presents some contributions when compared to the existing ap-
 70 proaches. Instead of simulating the sound pulse paths and the
 71 effects of their hits with the virtual objects, as presented by ray
 72 tracing and tube tracing-based methods [1, 2, 3, 4, 5, 6, 7], we
 73 take advantage of precomputed data (e.g., normals, distances,
 74 colors, angles) during the rasterization pipeline to compute the
 75 acoustic frame. In addition, all raster data are handled on GPU,
 76 accelerating then the simulation process with the guarantee of
 77 real-time response, in contrast to the methods found in [1, 2, 3,
 78 4]. Although the systems found in [1, 2, 3, 4, 5, 6, 7] focused
 79 on the simulation of specific sonar device, our simulator is able
 80 to reproduce two kinds of sonar devices: mechanical scanning
 81 imaging sonar (MSIS) and forward-looking sonar (FLS). The
 82 intensity measured back from the insonified objects depends
 83 on surface normal directions and reflectivity, producing more
 84 realistic simulated frames than binary representation, this lat-
 85 ter found in [5, 6]. The speckle noise is modeled as a non-
 86 uniform Gaussian distribution and applied to our final sonar
 87 image, which approaches to real-world sonar operation, differ-
 88 ently from [3, 4, 5, 6, 7]. On the other hand, we did not exploit
 89 the additive noise as it was considered in [3, 4]. Finally, it is
 90 noteworthy that our proposed system simulates physical phe-
 91 nomena since they are constrained to real-time (e.g. decision-
 92 making algorithms and control system tuning). Aware of this
 93 real-time constraint, the high computational cost phenomena
 94 such as reverberation is not included at this point, differently
 95 from [3, 7].

96 The main goal here is to build quality and low time-con-
 97 suming acoustic frames, according to underwater sonar image
 98 formation and operation modes (see Section 2). The pulse dis-
 99 tance, the echo intensity and the sonar field-of-view parameters
 100 are extracted from the underwater scene during the rasteriza-
 101 tion pipeline, and subsequently fused to generate the simulated
 102 sonar data, as described in Section 3. Qualitative and time eval-
 103 uation results for the two different sonar devices are presented
 104 in Section 4, allowing the use of the proposed simulator by real-
 105 time applications. Conclusions and future work are drawn in
 106 Section 5.

107 2. Imaging sonar operation

108 Sonars are echo-ranging devices that use acoustic energy to
 109 locate and survey objects in a desired area. The sonar trans-
 110 ducer emits pulses of sound waves (or ping) until they hit any
 111 object or are completely absorbed. When the acoustic signal
 112 collides with a surface, part of this energy is reflected, while
 113 other is refracted. The sonar data is built by plotting the echo
 114 measured back versus time of acoustic signal. The transducer
 115 reading in a given direction forms a *beam*. A single beam trans-
 116 mitted from a sonar is illustrated in Fig. 1. The horizontal and

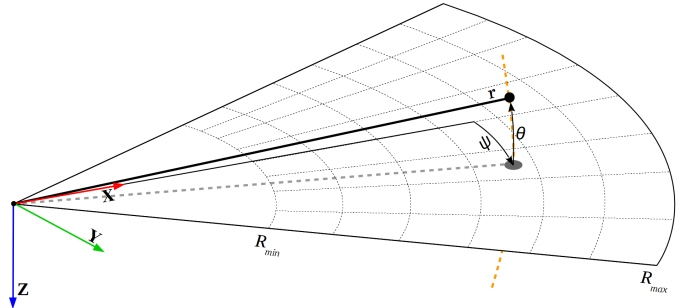


Figure 1: Imaging sonar geometry. By a projection process, all 3D points belonging to the same elevation arc (represented as dashed orange line) will be represented to the same image point in the 2D plane. Range r and azimuth angle ψ are measured, and elevation angle θ is lost. Sonar coverage area is defined by R_{min} and R_{max} .

117 vertical beamwidths are represented by the azimuth ψ and el-
 118 evation θ angles, respectively, where each sampling along the
 119 beam is named as *bin*. The sonar coverage area is defined by
 120 R_{min} and R_{max} . Since the speed of sound underwater is known,
 121 or can be measured, the time delay between the emitted pulses
 122 and the respective echoes (named as *time of flight*) reveals how
 123 far the objects are (distance r), as well as how fast they are mov-
 124 ing. The backscattered acoustic power in each bin determines
 125 the echo intensity value.

126 With different azimuth directions, the array of transducer
 127 readings forms the final sonar image. Since all incoming sig-
 128 nals converge to the same point, the reflected echoes could have
 129 been originated anywhere along the corresponding elevation arc
 130 at a fixed range, as depicted in Fig. 1. In the acoustic represen-
 131 tation, the 3D information is lost in the projection into a 2D
 132 image.

133 2.1. Sonar characteristics

134 Although sonar devices overcome main limitations of opti-
 135 cal sensors, they present more difficult data interpretation due
 136 to:

- 137 a) **Shadowing:** This effect is caused by objects blocking the
 138 sound waves transmission, and causing regions behind them,
 139 without acoustic feedback. These regions are defined by a
 140 black spot in the resulting sonar image, occluding part of
 141 the scene;
- 142 b) **Non-uniform resolution:** The amount of pixels used to
 143 represent an echo intensity record in the Cartesian coor-
 144 dinate system grows as its range increases. This situation
 145 causes image distortions and object flatness;
- 146 c) **Changes in viewpoint:** Imaging the same scene from dif-
 147 ferent viewpoints can cause occlusions, shadows move-
 148 ments and significant changes of observable objects [9].
 149 For instance, when an outstanding object is insonified, its
 150 shadow is shorter, as the sonar becomes closer;
- 151 d) **Low signal-to-noise ratio (SNR):** sonars suffer from low
 152 SNR mainly due the very-long-range scanning, and the
 153 presence of speckle noise introduced by acoustic wave in-
 154 terferences [10];

155 e) **Reverberation:** This phenomenon is caused when mul-
156 tiple acoustic waves, returning from the same object, are
157 detected over the same ping, producing duplicated objects.

158 2.2. Types of underwater sonar devices

159 The most common types of underwater acoustic sonars are
160 MSIS and FLS. In the former, the sonar image is built for each
161 pulse, with one beam per reading (see Fig. 2(a)); the resulting
162 sonar images in MSIS are usually depicted on a display pulse by
163 pulse, and the head position reader is rotated according to mo-
164 tor step angle. After a full 360° sector reading (or the desired
165 sector defined by left and right limit angles), the accumulated
166 sonar data is overwritten. The acquisition of a scanning image
167 involves a relatively long time, introducing distortions caused
168 by the vehicle movements. This sonar device is generally ap-
169 plied in obstacle avoidance [11] and navigation [12] applica-
170 tions. As illustrated in Fig. 2(b), the whole forward view of
171 an FLS is scanned and the current data is overwritten by the
172 next scanning in a high frame rate, with all beams being read
173 simultaneously; this is similar to a streaming video imagery for
174 real-time applications; this imaging sonar is commonly used
175 for navigation [13], mosaicing [9], target tracking [14] and 3D
176 reconstruction [15].

177 3. GPU-based sonar simulation

178 The goal of our work is to simulate two types of underwater
179 sonar with low computational cost. The complete pipeline of
180 the proposed simulator (from the virtual scene to the simulated
181 acoustic data) is detailed in the following sections. The sonar
182 simulator is written in C++ with OpenCV [16] support as Rock
183 packages.

184 3.1. Rendering underwater scene

185 In Rock-Gazebo framework [17], Gazebo handles with phys-
186 ical forces, while Rock's visualization tools are responsible by
187 the scene rendering. The graphical data in Rock are based
188 on OpenSceneGraph framework, an open source C/C++ 3D
189 graphics toolkit built on OpenGL. The osgOcean library is used
190 to simulate the ocean visual effects. In our case, Rock-Gazebo
191 integration provides the underwater scenario, allowing also real-
192 time hardware-in-the-loop simulation with a virtual AUV.

193 All scene aspects, such as world model, robot parts (includ-
194 ing sensors and joints) and other virtual objects are defined by
195 simulation description files (SDF), which use the SDFFormat
196 [18], an XML format used to describe simulated models and
197 environments for Gazebo. Visual and collision geometries of
198 vehicle and sensor robot are also described in specific file for-
199 mats. Each component described in the SDF file becomes a
200 Rock component, which is based on the Orococos real-time tool-
201 kit (RTT) [19], providing I/O ports, properties and operations
202 as communication layers. When the models are loaded, Rock-
203 Gazebo allows interaction between real world or simulated sys-
204 tem components with the simulated models. A resulting scene
205 sample of this integration is illustrated in Fig. 3.

206 3.2. Sonar rendering

207 A rendering pipeline can be customized by defining GPU
208 shaders. A shader is written in OpenGL Shading Language
209 (GLSL) [20], a high-level language with a C-based syntax, which
210 enables more direct control of graphics pipeline, avoiding the
211 use of low-level or hardware-specific languages. Shaders can
212 describe the characteristics of either a vertex or a fragment (a
213 single pixel). Vertex shaders are responsible by transforming
214 the vertex position into a screen position by the rasterizer, gen-
215 erating texture coordinates for texturing, and lighting the vertex
216 to determine each color. The rasterization results, in a set of
217 pixels to be processed by fragment shaders, manipulate pixel
218 location, depth and alpha values, and interpolated parameters
219 from the previous stages, such as colors and textures.

220 In our work, the underwater scenes are sampled by a virtual
221 camera (frame-by-frame), whose optical axis is aligned with the
222 **opening angle**, the intended **viewing direction** and the cover-
223 age **range** of the simulated sonar device (see Fig. 4(i)). To sim-
224 ulate the sonar imaging by using virtual camera frames, three
225 parameters are computed in fragment and vertex shaders, dur-
226 ing the rendering pipeline. This way, we are able to use the pre-
227 computed geometric information during the image rasterization
228 process on GPU. The three parameters to render the sonar de-
229 vice using a virtual camera are illustrated in Fig. 4(ii), and are
230 described as follows:

- 231 • **Pulse distance** simulates the time of flight of the acous-
232 tic pulse, being calculated by the Euclidean distance be-
233 tween the camera center and the object surface;
- 234 • **Echo intensity** represents the reflection of the acoustic
235 echo, calculated from the object surface normal regarding
236 the camera;
- 237 • **Sonar field-of-view** is represented by the camera field-
238 of-view in the horizontal direction.

239 By default, the shader encodes the raster data in 8-bit color
240 channels for red, green, blue and alpha (RGBA). In our simu-
241 lator, RGB channels are used to store the echo intensity, pulse
242 distance and sonar field-of-view parameters to render the sonar
243 from a virtual camera. The echo intensity parameter follows
244 a real sonar common representation as 8-bit values. The pulse
245 distance is replaced by the native GLSL 32-bit depth buffer to
246 avoid precision limitation during the calculation of the distance
247 histogram (see Fig. 4(iii)). As the field-of-view angle varies
248 from the image center to both side directions, the sonar field-
249 of-view is represented by 8-bit values without loss of precision.
250 All of these three parameters are normalized into the interval
251 $[0,1]$. For the echo intensity parameter, zero means no energy,
252 while one means maximum echo energy. For pulse distance,
253 the minimum value denotes a close object, while the maximum
254 value represents a far one, limited by the sonar maximum range.
255 Every sonar device has a maximum field-of-view; to represent
256 this parameter in the rendering pipeline, the zero angle is in the
257 center of the image, increasing until it reaches the half value of
258 the maximum field-of-view of the simulated sonar device, for
259 both sided borders; for example, if a sonar device has 120° of

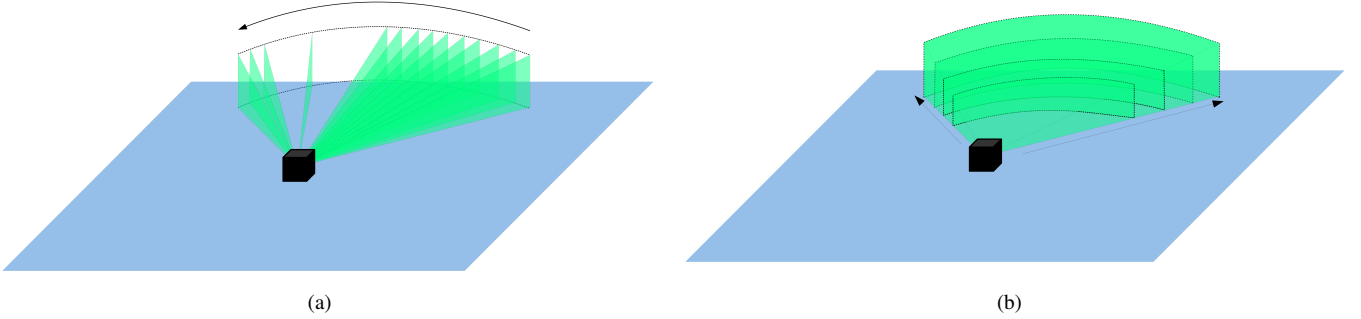


Figure 2: Different underwater sonar readings: (a) From a mechanical scanning imaging sonar and (b) from a forward-looking sonar.

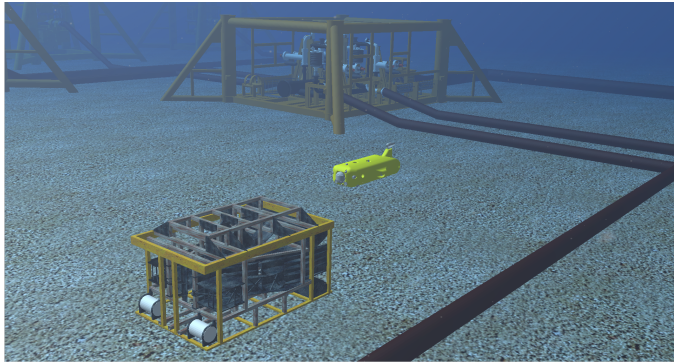


Figure 3: The AUV in Rock-Gazebo underwater scene.

260 field-of-view, the zero angle is in the center of the virtual cam-
261 era, spanning 60° to the right and 60° to the left.

262 In real-world sensing, surfaces usually present irregulari-
263 ties and different reflectance values. To render these surfaces
264 in a virtual scene, the echo intensity values can also be defined
265 by normal maps (see Fig. 5) and material property informa-
266 tion (see Fig. 6). Normal mapping is a rendering technique,
267 based on normal perturbation, that is used to simulate wrin-
268 kles and dents on the object surface by using RGB textures on
269 shaders. This approach consumes less computational resources
270 for the same level of detail, compared with the displacement
271 mapping technique, because the geometry remains unchanged.
272 Since normal maps are built in tangent space, interpolating the
273 normal vertex and the texture, tangent, bi-tangent and normal
274 (TBN) matrices are computed to convert the normal values into
275 the world space. The visual differences of applying normal
276 mapping in the actual scenes are illustrated in Figs. 5(a) and
277 5(c); in the shader representation, in Figs. 5(e) and 5(b); and
278 the final sonar image, in Figs. 5(d) and 5(f). The reflectance
279 allows properly describing the intensity received back from ob-
280 servable objects in shader processing, according to the material
281 properties (for instance, aluminum has more reflectivity than
282 wood and plastic). When an object has the reflectivity property
283 defined, the reflectance value ρ is passed to the fragment shader
284 and processed on GPU. So, the final pixel intensity represents
285 the product of surface normal angle by the reflectance value ρ .
286 The reflectance affects the shader representation, as depicted in
287 Figs. 6(a), 6(b), 6(c) and 6(d)), with a final sonar image shown

288 in Figs. 6(e), 6(f), 6(g) and 6(h).

289 3.3. Simulating operation of the sonar device

290 The sonar rendering parameters are used to compute the
291 corresponding acoustic representation. Since the sonar field-
292 of-view is radially spaced over the horizontal field-of-view of
293 the virtual camera (where all pixels in the same column have
294 the same angle), the first step is to split the image into a num-
295 ber of beams (beamed sub-images). Each column of the sonar
296 field-of-view parameter is related with a respective beam vector,
297 according to sonar bearings, as illustrated in Fig. 4(vi). In turn,
298 one beam represents one or more columns. Each beamed sub-
299 image is converted into bin intensities using the pulse distance
300 and the echo intensity parameters. In a real imaging sonar, the
301 echo measured back is sampled over time, and the bin number
302 is proportional to the sensor range. In other words, the initial
303 bins represent the closest distances, while the latest bins repre-
304 sent the farthest ones. Therefore a distance histogram (see Fig.
305 4(iii)) is computed in order to group the sub-image pixels with
306 the respective bins, according to the pulse distance parameter
307 and number of bins, and calculate the accumulated intensity in
308 each bin.

309 Due to the acoustic beam spreading and absorption in the
310 water, the final bins have less echo strength than the first ones.
311 This is so, because the energy is twice lost in the environment.
312 To tackle with that issue, sonar devices use an energy normal-
313 ization based on time-varying gain for range dependence com-
314 pensation, which spreads losses in the bins. In our simulation
315 approach, the accumulated intensity, I_{bin} , in each bin (see Fig.
316 4(iv)) is normalized as

$$317 \quad I_{bin} = \sum_{x=1}^N \frac{1}{N} \times S(i_x), \quad (1)$$

318 where x is the pixel location, N is the distance histogram value
319 (number of pixels) of that bin, $S(i_x)$ is a sigmoid function, and i_x
320 is the echo intensity value of the pixel x . \times defines an element-
321 wise multiplication.

322 Finally, the sonar image resolution must be big enough to
323 contain all information of the bins. For that, the number of bins
324 involved is directly proportional to the sonar image resolution.

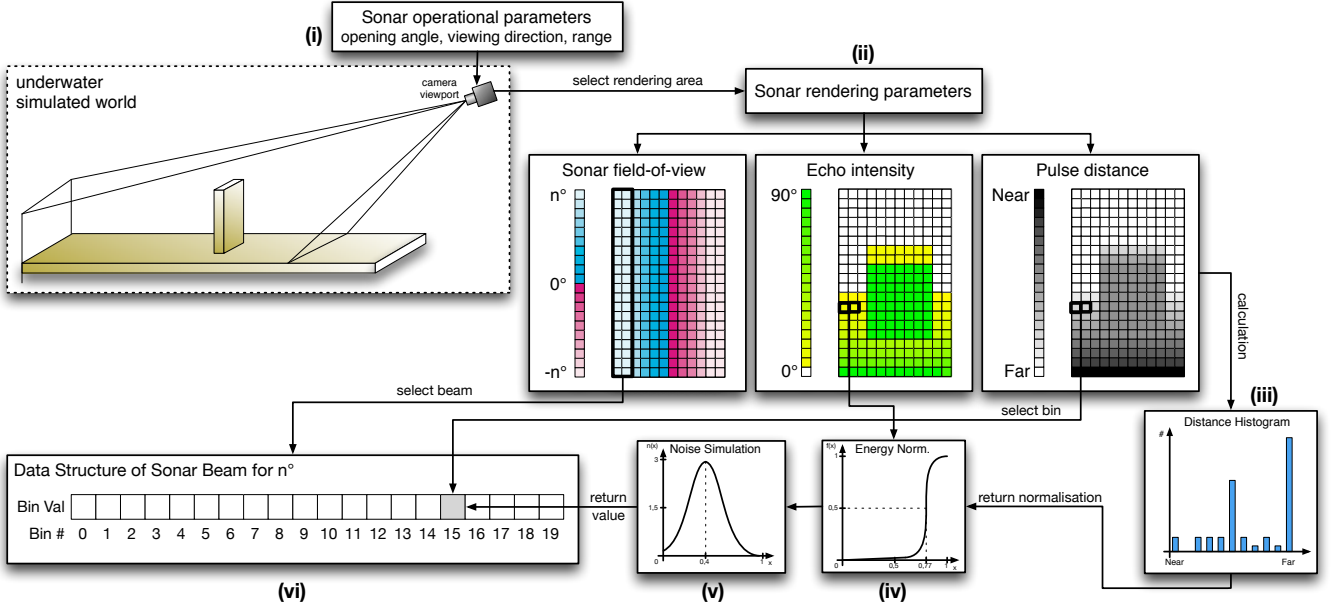


Figure 4: A graphical overview of the imaging sonar simulation process: (i) a virtual camera, specialized as the sonar device, samples the underwater scene; (ii) three 2D parameters are calculated by shader rendering on GPU: sonar field-of-view, echo intensity and pulse distance; the shader information is split into beam parts, according to the angle values, and the bin distance and echo intensity are defined by: (iii) distance histogram and (iv) energy normalization, respectively; (v) the speckle noise is applied to the final sonar data; (vi) and the simulated acoustic data is presented as Rock's data type.

3.3.1. Noise model

325 Imaging sonar systems are disturbed by a multiplicative noise
326 known as speckle, which is caused by coherent processing of
327 backscattered signals from multiple distributed targets. This
328 effect degrades image quality and visual evaluation. Speckle
329 noise results in constructive and destructive interferences, which
330 are shown as bright and dark dots in the image. The noisy im-
331 age has been expressed, following [21]:

$$333 \quad y(t) = x(t) \times n(t), \quad (2)$$

334 where t is the time instant, $y(t)$ is the noised image, $x(t)$ is the
335 free-noise image, $n(t)$ is the speckle noise matrix, and \times defines
336 an element-wise multiplication.

337 This type of noise is well-modeled as a Gaussian distribu-
338 tion. The physical explanation is provided by the central limit
339 theorem, which states that the sum of many independent and
340 identically distributed random variables tends to behave as a
341 Gaussian random variable [22]. A Gaussian distribution is de-
342 fined by following a non-uniform distribution, skewed towards
343 low values, and applied as speckle noise in the simulated sonar
344 image (see Fig. 4(v)). This noise simulation is repeated for
345 each virtual acoustic frame.

3.3.2. Integrating sonar device with Rock

347 After the imaging sonar simulation process, from the virtual
348 underwater scene to the representation of the degraded acous-
349 tic sonar data by noise, the resulting sonar data is encapsulated
350 as Rock's sonar data type (see Fig. 4(vi)). This data type is
351 provided as I/O port of a Rock's component, allowing the inter-
352 action with other simulated models and applications.

Table 1: Sonar device configurations used on experimental evaluation.

Device	# of beams	# of bins	Field of view	Down tilt	Motor Step
FLS	256	1000	120° x 20°	20°	-
MSIS	1	500	3° x 35°	0°	1.8°

354 To evaluate our simulator, experiments were conducted by
355 using a 3D model of an AUV equipped with an MSIS and an
356 FLS. Different scenarios were casted and studied, considering
357 the sonar device configurations summarized in Table 1. In the
358 experimental analysis, as the scene frames are being captured
359 by the sonars, the resulting acoustic images are sequentially
360 presented, on-the-fly (see Figs. 7 and 8).

361 4.1. Experimental evaluation

362 The virtual FLS from AUV was used to insonify the scenes
363 from three distinct scenarios. A docking station, in parallel with
364 a pipeline on the seabed, composes **the first scenario** (see Fig.
365 7(a)); the target surface is well-defined in the simulated acous-
366 tic frame (see Fig. 7(d)), as well as the shadows and speckle
367 noise; given that the docking station is metal-made, the texture
368 and reflectivity were set such that a higher intensity shape was
369 resulted in comparison with the other targets. **The second sce-**
370 **nario** presents the vehicle in front of a manifold model in a non-
371 uniform seabed (see Fig. 7(b)); the target model was insonified
372 to generate the sonar frame from the underwater scene (see Fig.
373 7(e)); the frontal face of the target, as well the portion of the

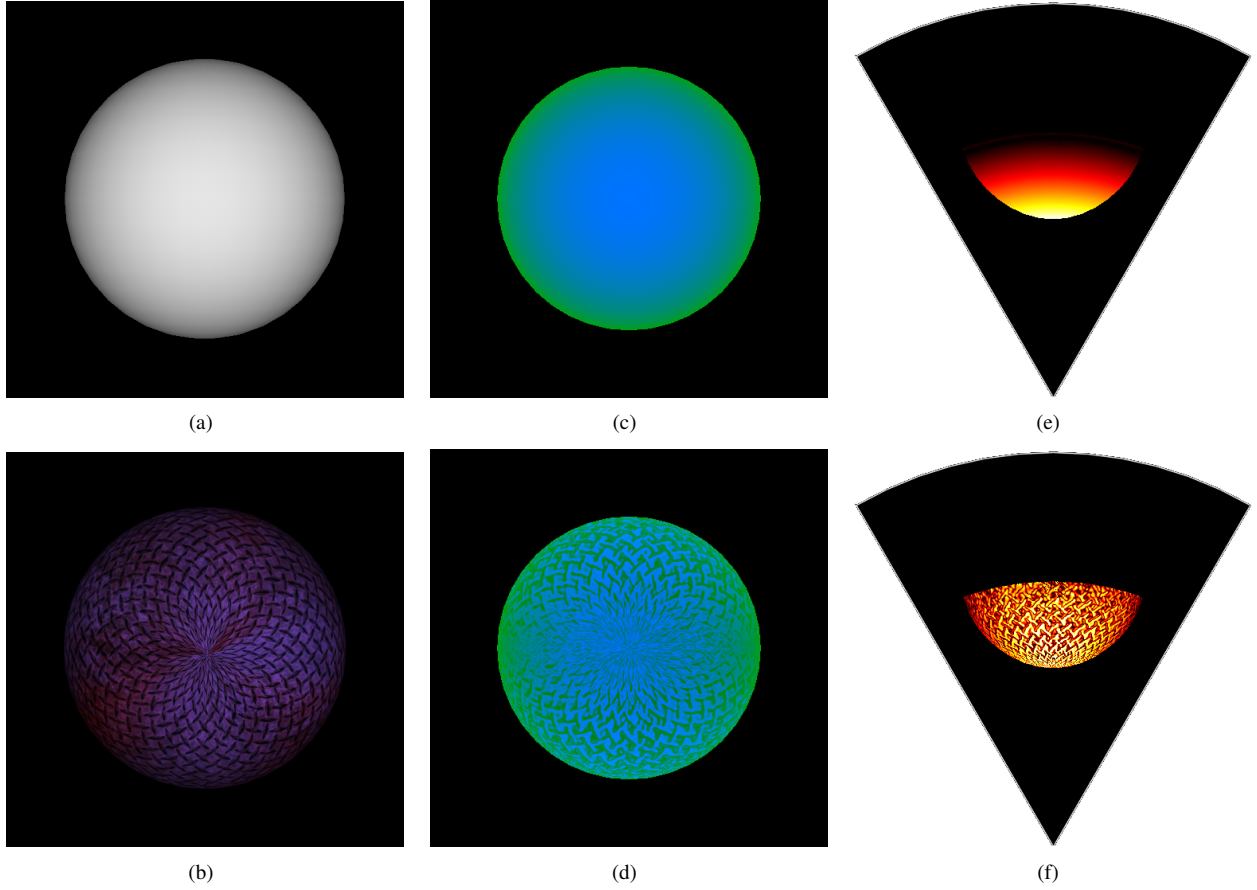


Figure 5: Example of shader rendering with normal mapping: A sphere without (a) and with texture (b); respective shader image representations of the spheres in (c) and (d), where the blue area represents the echo intensity parameter, while the green area represents the pulse distance parameter. The final acoustic images are depicted in (e) and (f). By using normal mapping technique, the textures changes the normal directions, and the sonar image details the appearance of object surface, like in real world sensing.

seabed and the degraded data by noise, are clearly visible in the FLS image; also, a long acoustic shadow is formed behind the manifold, occluding part of the scene. **The third scenario** contains a sub-sea isolation valve (SSIV) structure, connected to a pipeline in the bottom (see Fig. 7(c)); the simulated acoustic image, depicted in Fig. 7(f), also present shadows, material properties and speckle noise effects. Due to sensor configuration and robot position, the initial bins usually present a blind region in the three simulated scenes, caused by absence of objects at lower ranges, similar to real sonar images. It is noteworthy that the brightness of sea-floor decreases as it is farther from sonar, because of the normal orientation of the surface.

The MSIS was also simulated in three different experiments. The robot in a big textured tank composes **the first scene** (see Fig. 8(a)); similar to the first scenario of FLS experiment, the reflectivity and texture were set to the target; the rotation of the sonar head position, by a complete 360° scanning, produced the acoustic frame of tank walls (see Fig. 8(d)). **The second scene** involves the vehicle's movement during the data acquisition process; the scene contains a grid around the AUV (see Fig. 8(b)), captured by a front MSIS mounted horizontally; this trial induces a distortion in the final acoustic frame, because the relative sensor position with respect to the surrounding object

changes, as the sonar image is being built (see Fig. 8(e)); in this case, the robot rotates 20° left during the scanning. **The last scene** presents the AUV over oil and gas structures on the sea bottom (see Fig. 8(c)); using an MSIS located in the back of the AUV with a vertical orientation, the scene was scanned to produce the acoustic visualization; as illustrated in Fig. 8(f), object surfaces present clear definition in the slice scanning of the sea-floor.

All the experimental scenarios was defined in order to provide enough variability of specific phenomena usually found in real sonar images, such as acoustic shadows, noise interference, surface irregularities and properties, distortion during the acquisition process and changes of acoustic intensities. However, the speckle noise application is restricted to regions with acoustic intensity, as shown in Figs. 7(f) and 8(d). This fact is due to our sonar model be multiplicative (defined in Eq. 2). In real sonar images, the noise also granulates the shadows and blind regions. The sonar simulator can be improved by inserting an additive noise to our model. The impact of incorporating additive noise on the image is more severe than that of multiplicative, and we decided to collect more data before including a specific additive noise in our simulator, at this moment. A second feature missing in our simulated acoustic images are the ghost effects

Table 2: Processing time to generate forward-looking sonar samples with different parameters.

# of samples	# of beams	# of bins	Field-of-view	Average time (ms)	Std dev (ms)	Frame rate (fps)
500	128	500	120° x 20°	54.7	3.7	18.3
500	128	1000	120° x 20°	72.3	8.9	13.8
500	256	500	120° x 20°	198.7	17.1	5.0
500	256	1000	120° x 20°	218.2	11.9	4.6
500	128	500	90° x 15°	77.4	11.8	12.9
500	128	1000	90° x 15°	94.6	10.2	10.6
500	256	500	90° x 15°	260.8	18.5	3.8
500	256	1000	90° x 15°	268.7	16.7	3.7

Table 3: Processing time to generate mechanical scanning imaging sonar samples with different parameters.

# of samples	# of bins	Field-of-view	Average time (ms)	Std dev (ms)	Frame rate (fps)
500	500	3° x 35°	8.8	0.7	113.4
500	1000	3° x 35°	34.5	1.6	29.0
500	500	2° x 20°	10.3	0.6	96.7
500	1000	2° x 20°	41.7	3.7	24.0

420 caused by reverberation. This lacking part can be addressed by 421 implementation of a multi-path propagation model [23], where 422 the signal propagates along several different paths, resulting in 423 fading and reverberation effects. Simulating the multi-path re- 424 flection is computationally costly, thus we need more time to 425 modeling and including the reverberation phenomenon, to con- 426 sider the real-time constraints.

427 4.2. Computational time

428 Performance evaluation of the simulator was assessed by 429 considering the suitability to run real-time applications. The 430 experiments were performed on a Intel Core i7 3540M proces- 431 sor, running at 3 GHz with 16GB DDR3 RAM memory and 432 NVIDIA NVS 5200M video card, with Ubuntu 16.04 64 bits 433 operating system. The elapsed time of each sonar data is stored 434 to compute the average time, standard deviation and frame rate 435 metrics, after 500 iterations. The results found is summarized in 436 Tables 2 and 3. After changing the sonar rendering parameters, 437 such as number of bins, number of beams and field-of-view, 438 the proposed approach generated the sonar samples with a high 439 frame rate, for both sonar types, in comparison to real-world 440 sonars. For instance, the Tritech Gemini 720i, a real forward- 441 looking sonar sensor, with a field-of-view of 120° by 20° and 442 256 beams, presents a maximum update rate of 15 frames per 443 second; so, the obtained results allow the use of the sonar sim- 444 ulator for real-time applications. Also, the MSIS data used in 445 the simulator is able to complete a 360° scan sufficiently fast in 446 comparison with a real sonar as Tritech Micron DST. For the 447 FLS device, these rates are superior to the rates lists by De- 448 Marco *et al* [4] (330ms) and Saç *et al* [3] (2.5min). For MSIS 449 type, to the best of our knowledge, there is no previous work 450 for comparison.

451 According to previous results, since the number of bins is 452 directly proportional to sonar image resolution, we can con- 453 clude that the number of bins used affects the computational 454 time; when the number of bins increases, the simulator will 455 have a bigger scene frame to compute and to generate the sonar 456 data.

457 4.3. Quality evaluation of the simulated sonar image

458 Numerically assessing the performance of a sonar simulator 459 is a non-trivial task. As sonar simulators must work as trustwor- 460 thy environment to avoid in-field experiments, the goal of the 461 quantitative evaluation should be to demonstrating that the real- 462 world sonar image can be aligned with the synthetic one. Just 463 two out of the six works analyzed in Section ?? perform quan- 464 titative evaluation of the proposed simulators, but only with re- 465 spect to computational time.

466 Image alignment must be carried out by considering a real- 467 world and a virtual scene, both insonified by real and virtual 468 sonar devices, respectively, in the exact same conditions. In 469 other words, same conditions mean that we have to guarantee 470 the same pose of the AUV in the real and virtual scenarios, 471 which, in turn, should present the same elements being insoni- 472 fied; measuring the alignment of the images (real and virtual) 473 works as comparing how much the simulated sonar image is 474 similar to the real one with respect to pixel intensity and loca- 475 tion.

476 The process of measuring the alignment (similarity) of two 477 images can be performed by a set of measures, such as: mutual 478 information, entropy, peak signal-to-noise ratio (PSNR), struc- 479 tural similarity index measure (SSIM), and interesting point de- 480 tectors and distances (*e.g.*, scale invariant feature transform - 481 SIFT). To evaluate the alignment between the real and virtual 482 images, we attempted to model a real scene insonified by our

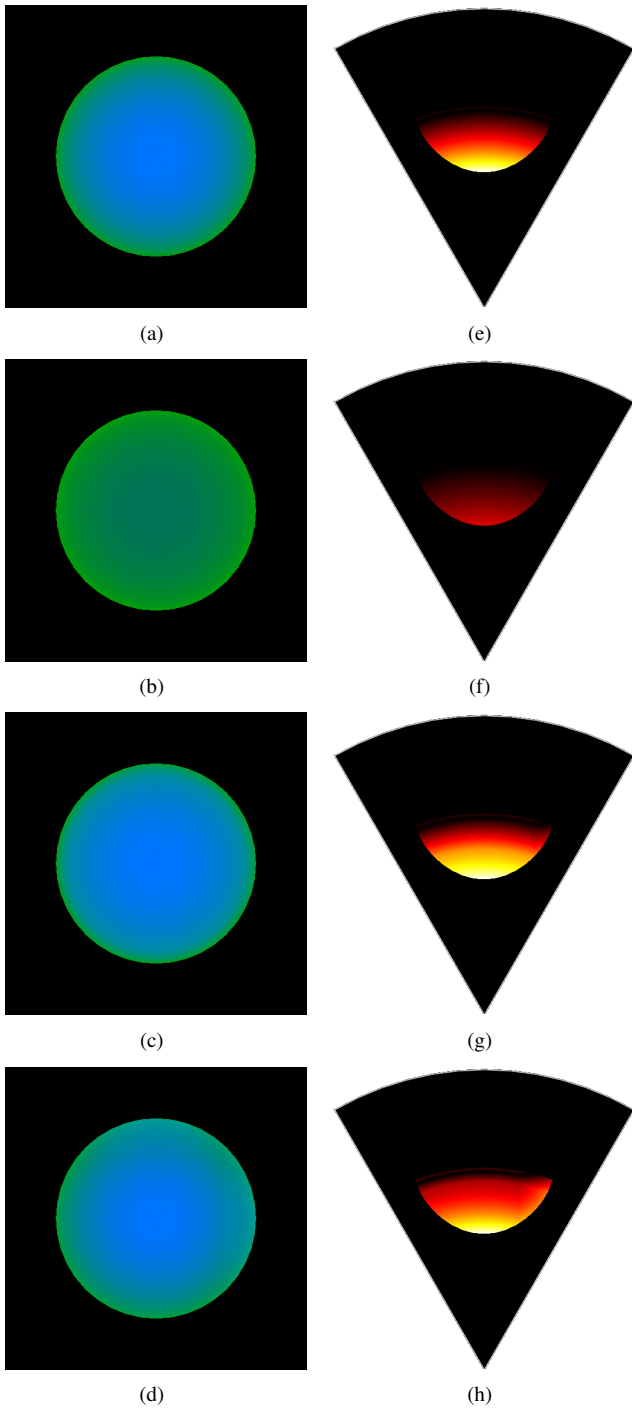


Figure 6: Examples of different reflectance values, ρ , applied in shader image representation of the same target, where blue is the echo intensity parameter and green is the pulse distance parameter: (a) raw image; (b) $\rho = 0.35$; (c) $\rho = 1.40$; and (d) $\rho = 2.12$. The following acoustic images are presented in (e), (f), (g) and (h).

489 of similarity between each pair of images.

490 5. Conclusion and future work

491 A GPU-based simulator for imaging sonar was proposed
 492 here. The system is able to reproduce the operation mode of two
 493 different types of sonar devices (FLS and MSIS) in real-time.
 494 The real sonar image singularities, such as multiplicative noise,
 495 surface properties and acoustic shadows are addressed, and rep-
 496 resented in the simulated frames. Specially for the shadows, the
 497 acoustic representation can present information as useful as the
 498 insonified object. Considering the qualitative results, the sonar
 499 simulator can be used by feature detection algorithms, based
 500 on corners, lines and shapes. Also, the computational time to
 501 build one sonar frame was calculated using different device set-
 502 tings. The vertex and fragment processing during the underwa-
 503 ter scene rendering accelerates the rendered sonar image, pro-
 504 viding an average time close or better than real-world imaging
 505 devices. These results allow the use of this imaging sonar sim-
 506 ulator by real-time applications, such as obstacle detection and
 507 avoidance, and object tracking. We are working now on a way
 508 to add the reverberation effect to perform a more close-to-real
 509 sensing, without significantly affecting the computational time.
 510 We are also working on how to include an additive noise in the
 511 simulation of the acoustic images. Future works will focus on
 512 qualitative and time consuming comparison with other sonar
 513 simulators and with real acoustic images.

514 References

- 515 [1] Bell JM. Application of optical ray tracing techniques to the simulation
 516 of sonar images. *Optical Engineering* 1997;36(6):1806–13.
- 517 [2] Coiras E, Groen J. Simulation and 3d reconstruction of side-looking sonar
 518 images. In: Silva S, editor. *Advances in Sonar Technology*; chap. 1. In-
 519 Tech; 2009, p. 1–15.
- 520 [3] Saç H, Leblebicioğlu K, Bozdağı Akar G. 2d high-frequency
 521 forward-looking sonar simulator based on continuous surfaces ap-
 522 proach. *Turkish Journal of Electrical Engineering and Computer Sciences*
 523 2015;23(1):2289–303.
- 524 [4] DeMarco K, West M, Howard A. A computationally-efficient 2d imag-
 525 ing sonar model for underwater robotics simulations in Gazebo. In:
 526 MTS/IEEE OCEANS Conference. 2015, p. 1–8.
- 527 [5] Gu J, Joe H, Yu SC. Development of image sonar simulator for under-
 528 water object recognition. In: MTS/IEEE OCEANS Conference. 2013, p.
 529 1–6.
- 530 [6] Kwak S, Ji Y, Yamashita A, Asama H. Development of acoustic camera-
 531 imaging simulator based on novel model. In: IEEE International Con-
 532 ference on Environment and Electrical Engineering (EEEIC). 2015, p.
 533 1719–24.
- 534 [7] Guériot D, Sintes C. Forward looking sonar data simulation through tube
 535 tracing. In: MTS/IEEE OCEANS Conference. 2010, p. 1–6.
- 536 [8] Quigley M, Conley K, Gerkey BP, Faust J, Foote T, Leibs J, et al. ROS:
 537 an open-source robot operating system. In: Workshop on Open Source
 538 Software, held at IEEE International Conference on Robotics and Auto-
 539 mation (ICRA). 2009, p. 1–6.
- 540 [9] Hurtós N. Forward-looking sonar mosaicing for underwater environments.
 541 Ph.D. thesis; Universitat de Girona; 2014.
- 542 [10] Abbot J, Thurstone F. Acoustic speckle: theory and experimental analy-
 543 sis. *Ultrasonic Imaging* 1979;1(4):303–24.
- 544 [11] Ganesan V, Chitre M, Brekke E. Robust underwater obstacle detection
 545 and collision avoidance. *Autonomous Robots* 2015;40(7):1–21.
- 546 [12] Ribas D, Rida P, Neira J. Underwater SLAM for structured environ-
 547 ments using an imaging sonar. Springer-Verlag Berlin Heidelberg; 2010.

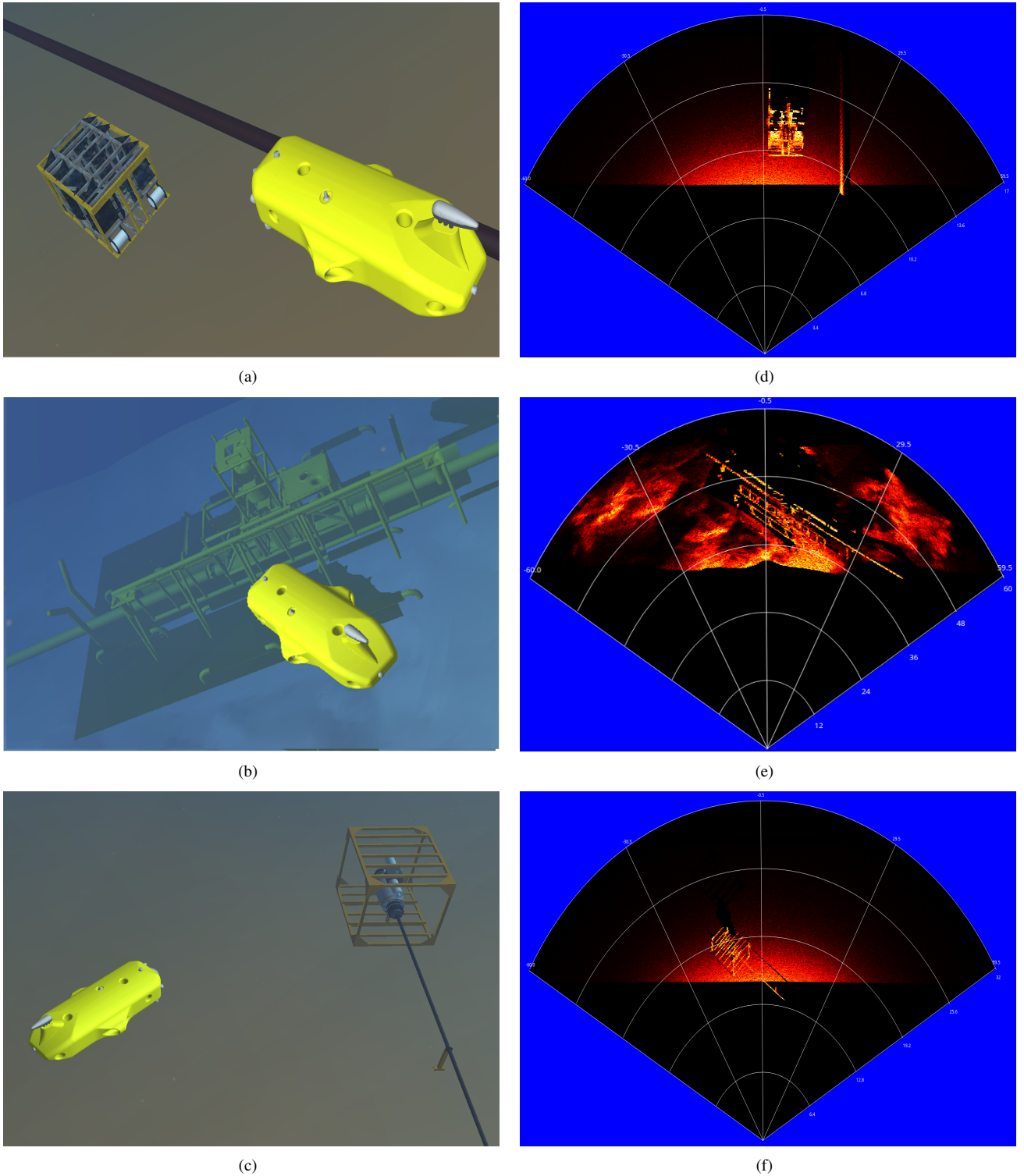


Figure 7: Forward-looking sonar simulation experiments: (a), (b) and (c) present the virtual underwater trials, while (d), (e) and (f) are the correspondent acoustic representations of each scenario, respectively.

- 548 [13] Fallon MF, Folkesson J, McClelland H, Leonard JJ. Relocating under- 549 water features autonomously using sonar-based SLAM. *Journal of Ocean* 550 *Engineering* 2013;38(3):500–13.
- 551 [14] Liu L, Xu W, Bian H. A LBF-associated contour tracking method for 552 underwater targets tracking. In: MTS/IEEE OCEANS Conference. 2016, 553 p. 1–5.
- 554 [15] Huang TA, Kaess M. Towards acoustic structure from motion for imaging 555 sonar. In: IEEE/RSJ International Conference on Intelligent Robots and 556 Systems (IROS). 2015, p. 758–65.
- 557 [16] Bradski G. The opencv library. *Doctor Dobbs Journal* 2000;25(11):120– 558 6.
- 559 [17] Watanabe T, Neves G, Cerqueira R, Trocoli T, Reis M, Joyeux S, et al.

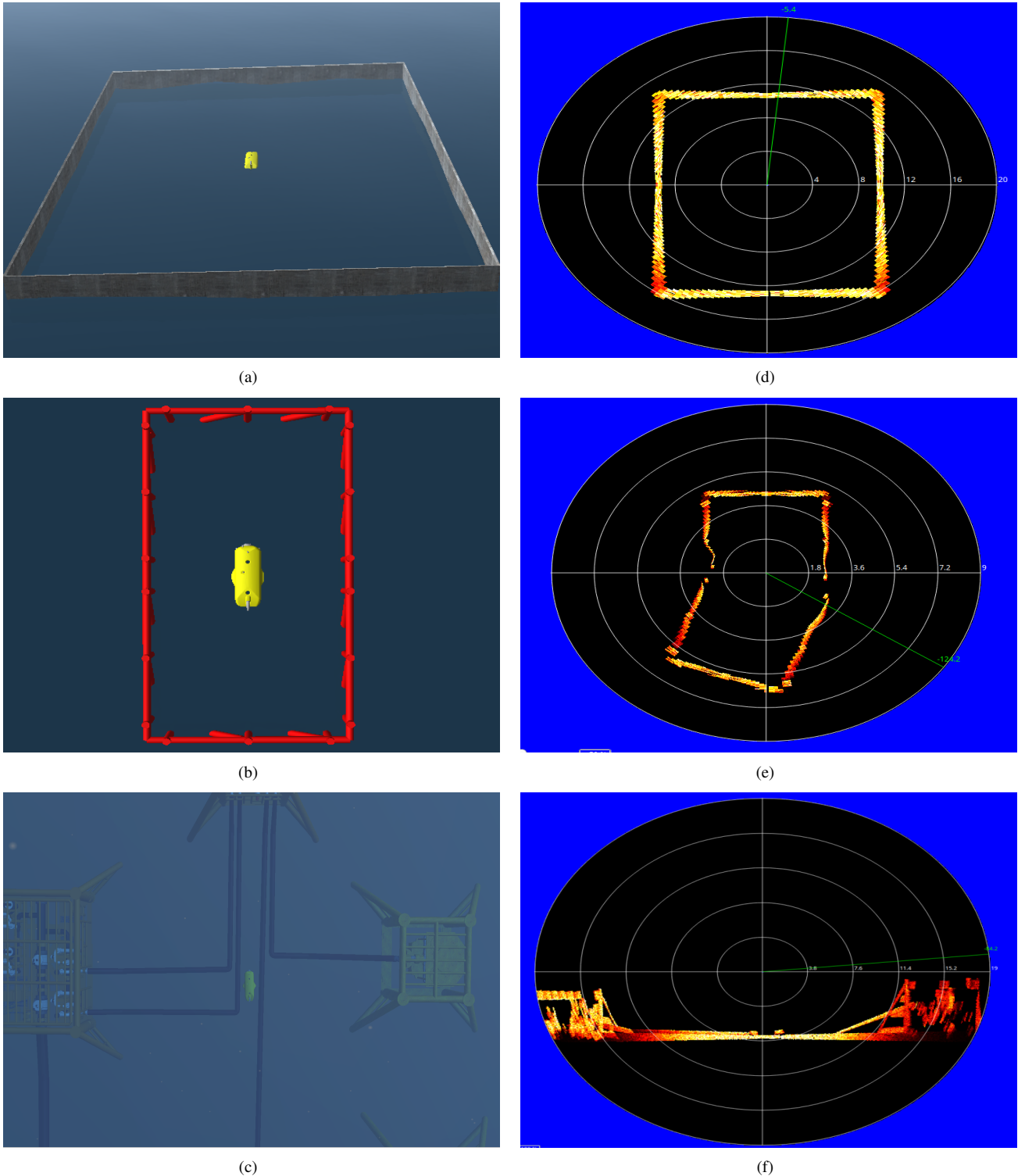


Figure 8: Experiments using mechanical scanning imaging sonar in three different scenarios (a), (b) and (c), and the respective processed simulated frames in horizontal orientation in (d) and (e), and vertical orientation in (f).

- 560 The Rock-Gazebo integration and a real-time AUV simulation. In: IEEE 566 [20] Rost RJ, Licea-Kane B, Ginsburg D, Kessenich JM, Lichtenbelt B, Malan
561 Latin American Robotics Symposium (LARS). 2015, p. 132–8. 567 H, et al. OpenGL shading language. 3rd ed.; Addison-Wesley Profes-
562 [18] SDF. <http://sdformat.org/>; 2017. Accessed: 2017-04-23. 568 sional; 2009.
563 [19] Soetens P, Bruyninckx H. Realtime hybrid task-based control for robots 569 [21] Lee J. Digital image enhancement and noise filtering by use of local
564 and machine tools. In: IEEE International Conference on Robotics and 570 statistics. IEEE Transactions on Pattern Analysis and Machine Intelligence
565 Automation (ICRA). 2005, p. 260–5. 571 1980;2(2):165–8.

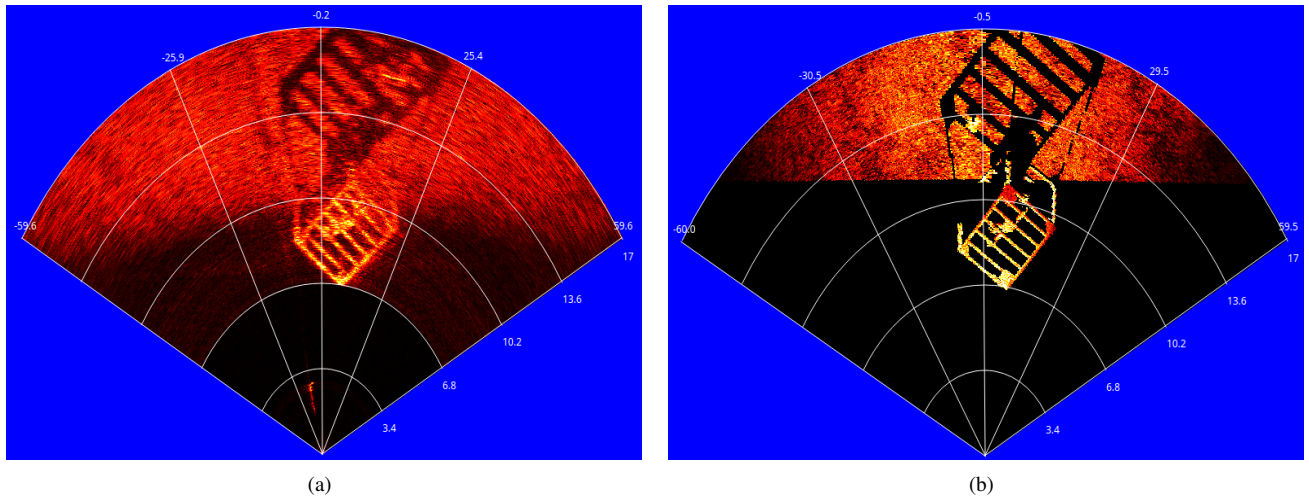


Figure 9: XXXXXXXXXXXXXXXXX.

- 572 [22] Papoulis A, Pillai S. Probability, random variables and stochastic pro-
573 cesses. McGraw Hill; 2002.
574 [23] Huang J. Simulation and modeling of underwater acoustic communica-
575 tion channels with wide band attenuation and ambient noise. Ph.D. thesis;
576 Carleton University; 2015.